GSA Data Repository 2018170

Super et al., 2018, North Atlantic temperature and pCO2 coupling in the early-middle Miocene: Geology, https://doi.org/10.1130/G40228.1.

SUPPLEMENTAL METHODS

Samples

Biomarkers, including Glycerol Dialkyl Glycerol Tetraethers (GDGTs) and alkenones, were measured in retained polar fractions from a previous study on Ocean Drilling Program Site 608 (n = 145; Pagani et al., 1999), and in additional samples from the same site requested from IODP in 2017 (n = 35)**.** The carbon and oxygen isotopes of planktonic foraminifera and the carbon isotopes of alkenones were previously analyzed in the stored samples (Pagani et al., 1999). Additional samples were selected to both minimize the effect of a coring gap (302 to 312 mbsf), and to test whether long-term laboratory storage affected GDGT and alkenone abundances.

Lipid Extraction and Preparation

Samples obtained in 2017 were freeze-dried, homogenized using a mortar and pestle, followed by lipid extraction with a Dionex 300 Accelerated Solvent Extractor (ASE) using a solvent mixture of dichloromethane/methanol (2:1, v/v). Total lipid extracts were separated into compound classes using silica gel chromatography with an elution series of hexane, dichloromethane and then methanol, resulting in, respectively, aliphatic, aromatic (containing alkenones) and polar (containing GDGT) fractions. Stored polar fractions were originally collected for the Pagani et al. (1999) study using silica gel chromatography methods following soxhlet extraction (see Pagani et al. (1999) for detailed methodology). ASE and soxhlet

extraction produce similar results when extracting core GDGTs used for the indices used in this study (Lenneger et al., 2012). Freshly extracted polar fractions and those taken from storage were passed through activated basic Al_2O_3 columns using dichloromethane/methanol (1:1; v/v) in a further purification step (Schouten et al., 2007). All samples were dissolved in hexane/2-propanol (99:1; v/v) and passed through a 0.45 μm PTFE filter prior to analysis.

GDGT Analysis

Filtered polar fractions were analyzed for GDGTs using an Agilent 1200 High-Performance Liquid Chromatograph (HPLC) system coupled to a 6130 quadrupole mass selective detector. Compounds were separated using a Cyano column (2.1 × 150 mm, 1.7 μm; Grace), fitted with a 2.1 × 5 mm pre-column of the same material, in a column compartment maintained at 30°C (Hopmans et al., 2006). Samples were eluted isocratically for 5 min with a mobile phase of 99:1 hexane/2-propanol (v/v) followed by a linear gradient to 96:4 hexane/2-propanol (v/v) for 50 min. Total run time was 76 minutes, including 10 minutes backflushing with 90:10 hexane/2-propanol (v/v) and 16 minutes for re-equilibration. Flow rate was 0.2 ml/min and maximum back pressure was 30-35 bars. Total run time was 76 minutes, including 10 minutes for re-equilibration. GDGTs were detected using selective ion monitoring of the protonated molecules $[M+H]^+$ (measured m/z: 744, 1018, 1020, 1022, 1032, 1034, 1036, 1046, 1048, 1050, 1292, 1294, 1296, 1298, 1300, 1302). with Atmospheric Pressure Chemical Ionization (APCI) source conditions as in Schouten et al. (2007). A synthetic C46 standard of known concentration was added for quantification and GDGT elution times were determined using an internal laboratory standard (Huguet et al., 2006). TEX_{86} reproducibility was ~0.01 TEX_{86} units based on the

reproducibility of an in-house standard and the instrument response factor was assumed to be the same for all isoprenoidal and branched GDGTs (Zhang et al., 2014).

Alkenone Analysis

New and stored aromatic fraction samples were evaluated for alkenones. $U^{k'}_{37}$ had not been determined in the original Pagani et al. (1999) study, due to low concentration of the tri-unsaturated alkenone (37:3) presumed to be the result of diagenetic alteration or uncertain application of the Uk'37 calibration to the Miocene. These assumptions were reassessed with concentrated runs of stored and newly extracted aromatic fractions, which yielded sufficient abundance for calculation of $U^{k'}_{37}$ from some samples. Analysis was conducted on an Agilent 7890B Gas Chromatograph (GC) fitted with a flame ionization detector (FID) and a Restek Rxi-1ms capillary column (60 m x 0.25 mm i.e., 0.25 μm film thickness). Using helium as the carrier gas (constant flow rate of 2.0 mL/min), the temperature program ramped at ramped from 90°C to 320°C at 15°C/min, followed by an isothermal hold for 15 min (Zhang et al., 2013). The ratio of the di-unsaturated alkenone (37:2) to the tri-unsaturated alkenone (37:3) was evaluated relative to an internal *n*-alkane standard (*n*-C38) (Zhang et al., 2014).

GDGT INDICES AT SITE 608

TEX_{86} Calibration

The BAYSPAR TEX_{86} calibration of Tierney and Tingley (2015) is used in this study to estimate sea surface temperatures, which are used in the alkenone pCO_2 calculation. We choose this regionally varying, Bayesian calibration in place of the widely applied logarithmic TEX_{86}^{H}

calibration (Kim et al., 2010) as it more fully accounts for trends in the residuals between observed and TEX_{86}-estimated SSTs in modern coretops. A comparison of the two calibrations (DR4) shows that TEX_{86}^{H} consistently predicts lower temperatures in the warmer part of the record (maximum difference of ~3°C), while BAYSPAR and TEX_{86}^{H} are similar (l relative to the cooler part of the record (average difference <1°C).

GDGT Source Proxies

Interpreting TEX_{86} values as a sea surface temperature proxy relies upon the assumption that the principal pelagic source of GDGTs in the modern ocean is the membrane lipids of marine Thaumarcheota, and that the same was true for the past (Schouten et al., 2013). The input of isoprenoidal GDGTs from other archaea can influence the temperature signal and can be assessed using the following GDGT-based indices:

1. The Branched and Isoprenoid Tetraether (BIT) index is a parameter that evaluates the proportion of branched GDGTs, thought to be primarily produced by soil bacteria (Weijers et al., 2007). BIT values >0.3 may indicate a significant terrestrial influence on marine samples, though evidence of *in situ* production of branched GDGTs in (particularly anoxic) marine environments and the preferential preservation of branched GDGTs relative to isoprenoidal GDGTs during oxic degradation makes the interpretation of BIT values site-dependent (Hopmans et al., 2006; Huguet et al., 2008; Smith et al., 2012; De Jonge et al., 2014; Weijers et al., 2014; Xiao et al., 2016). Given the distal location of Site 608 from land, significant terrigenous input at this site seems unlikely (Pagani et al., 2000; Kim et al., 2014). Absence of significant terrigenous input is indicated by sedimentological and

biomarker evidence (Pagani et al., 2000). In particular, *n*-alkane distributions are dominated by medium chain lengths indicative of algae and bacteria, with higher chain lengths (*n*-C27 *n*-C33) associated with terrestrial plants present but less abundant (Pagani et al., 2000). These *n*-alkane profiles suggest some terrestrial input to the site, but aeolian dust transport has not been shown to transport significant quantities of GDGTs to distal sites off modern North-west Africa (Fietz et al., 2009). The lack of evidence of terrestrial organic matter input suggests that the elevated BIT values reflect the combined effects of *in-situ* branched GDGT production, and/or differential preservation of branched and isoprenoidal GDGTs. Furthermore, the lack of a statistically significant correlation between TEX86 and BIT throughout the record further suggests that BIT in our record does not indicate biased TEX_{86} SST estimates (DR5-6).

2. The Methane Index (MI) detects isoprenoidal GDGT input from methanotrophic Euryarchaeota, with values >0.5 indicating potentially compromised TEX_{86} results (Zhang et al., 2011). Use of this threshold results in the exclusion of 2 data points from the SST record at ~ 19 Ma (Fig. DR5-6). The lack of a statistically significant correlation between MI and TEX_{86} throughout the record also suggests that, in general, variation in MI does not indicate biased TEX_{86} SST estimates.
3. The Δ Ring Index reflects the difference of the measured Ring Index (i.e. the weighted average number of rings in the isoprenoidal GDGTs, including the two most abundant compounds excluded from the TEX_{86} formulation, GDGT-0 and Crenarcheol) and the Ring Index predicted from the measured TEX_{86} based on the relationships of TEX_{86} and Ring Index in the modern ocean. Higher values indicate that the sample distribution may reflect an archaeal community distinct from the modern (Zhang et al., 2016). The exact threshold

above which TEX_{86} SST estimates are biased is unclear, however, due to an incomplete understanding of the the mechanisms responsible for variations in the index. We do not use Δ Ring Index to exclude additional samples at Site 608 but note that the interval with the highest Δ Ring Index values occurs ~19.5 to 17 Ma, an interval where we also see other indicators of variations in GDGT provenance (DR5-6).

4. Higher ratios of GDGT-2/GDGT-3 are correlated with deeper water and, presumably, a larger contribution of GDGTs from deeper in the water column, based on a modern global compilation of marine sites (Taylor et al., 2013). It is unlikely that water depth changed significantly at Site 608 during the Miocene, suggesting that variations in GDGT-2/GDGT-3 (DR4) at least in part may reflect changes in the contribution of GDGTs from deeper in the water column, particularly during the interval from 19.5 to 17 Ma. While deeper dwelling Archaea can have give apparent apparently higher TEX_{86} temperatures despite lower ambient temperatures (Lengger et al., 2014), the similarity in TEX_{86} temperatures in the interval with suspect values to the immediately preceding and following intervals suggests that deeper production did not significantly bias the record (Zell et al., 2015) (DR7).

ALKENONE pCO_2 PROXY

Alkenone pCO_2 Calculation and Assumptions

The alkenone pCO_2 proxy is based on:

$$\varepsilon_{p37:2} = \varepsilon_f - b/[CO_{2aq}] \quad (1)$$

where '*b*' represents the combination of physiological factors including growth rate and cell geometry that affect carbon isotope discrimination of the haptophyte algae cell. ε_f represents carbon isotope fractionation due to all carbon-fixing reactions, and is assumed to be 25‰ in this study following Zhang et al. (2013). $\varepsilon_{p37:2}$ represents the carbon isotope fractionation between aqueous CO_2 ($[CO_{2aq}]$) and the algal cell:

$$\varepsilon_{p37:2} = [(\delta CO_{2aq} + 1000)/((\delta_{org} + 1000) - 1)]*1000 \quad (2)$$

where δ_{org} represents the carbon isotope composition the entire cell, calculated using the carbon isotope composition of the di-unsaturated alkenone ($\delta_{37:2}$) (values from Pagani et al., 1999):

$$\delta_{org} = [(\delta_{37:2} + 1000)*((4.2/1000) + 1)] - 1000 \quad (3)$$

δCO_{2aq} (i.e., the $\delta^{13}C$ of total dissolved inorganic carbon (DIC)) is approximated using the $\delta^{13}C$ of surface dwelling planktonic foraminifera, assuming isotopic chemical equilibrium between the foraminiferal calcite and DIC. Foraminiferal $\delta^{13}C$ used in this study is from Pagani et al. (1999), measured on surface dwelling *Globigerinoides* spp. (including both *Globigerinoides trilobus* and *Globigerinoides quadrilobatus*). The aqueous carbon species are assumed to be in equilibrium with atmospheric pCO_2. Assuming a '*b*' factor based on a modern correlation to nutrient levels represented by $[PO_4^{3-}]$ (μM):

$$[CO_{2aq}] = (118.52*[PO_4^{3-}] + 84.07)/(\varepsilon_f - \varepsilon_{p37:2}) \quad (4)$$

A range of $[PO_4^{3-}]$ from 0.2 to 0.3 μMol, based on the modern variability in the top 100 m at Site 608 was used in this study. $[CO_{2aq}]$ is converted using Henry's Law:

$$pCO_2 = [CO_{2aq}] / k_H \quad (5)$$

with atmospheric pCO_2 in parts per million per volume (ppmv) and where:

$$k_H = (-0.00004*T^3 + 0.0048*T^2 - 0.2313*T + 6.2665)/100 \quad (6)$$

with 'T' representing a proxy sea surface temperature such as TEX_{86}^{H}. The equation assumes a constant salinity of 35‰ (Weiss, 1974). The analytical and calibration uncertainty of each parameter is reflected in the plotted pCO_2 range.

Two assumptions in the calculation of the alkenone pCO_2 proxy may not have been valid through the entire record at Site 608:

1. Carbon concentrating mechanisms (CCMs) were likely utilized by alkenone producers in the middle to late Miocene (Bolton et al., 2013), which would result in lower apparent pCO_2 estimates. Bolton et al. (2016) demonstrate that the prevalence of CCMs, inferred from the size and $\delta^{13}C$ of coccoliths, starting at approximately 8 Ma at Site 925 in the equatorial Atlantic and Site 999 in the Caribbean, later than the analytical window of this study, suggesting that CCMs and their attendant complications do not impact the Site 608 record. It is likely that both of these factors may have influenced the record, though, and further work is needed to fully explore these factors.
2. The assumption that the '*b*' term in (1) can constrained based on a modern range of $[PO_4^{3-}]$ at Site 608 may be incorrect. Sharply varying sediment and organic carbon accumulation rates (Diester-Haass et al., 2009) as well as intervals with low biomarker abundance suggest that primary and export productivity, as well as haptophyte algal growth rates, may have varied **(**DR**5).** High - low *p*CO2 estimates from ~19.5 to 17 Ma may reflect low - high haptophyte growth rates distinct from the rest of the record, based on high-low $\varepsilon_{p37:2}$ values not present at other lower Miocene sites (Pagani et al., 1999). The interval also had the highest Methane Index, Δ Ring Index and the lowest GDGT-2/GDGT-3 of the record, indicative of greater methanotrophic archaeal activity lower in

the water column, likely related to shifting nutrient regimes in the surface ocean, though this interpretation is qualitative (DR6-8). For Site 608, data on the size of coccoliths are not available, making the role of growth rate variation difficult to assess (Henderiks and Pagani, 2007; Zhang et al., 2013). Like CCMs, further work is needed to better understand the effect of growth rate at Site 608.

Alkenone pCO_2 Error Propagation

Analytical and calibration uncertainty was propagated through the pCO_2 calculation using a Monte Carlo approach.

First, 10,000 simulated SSTs for each data point were output using the Analog BAYSPAR MatLab script (Tierney and Tingley, 2015). These data were used to construct the 68% and 95% confidence interval plotted in Fig. 2. Planktic foraminiferal SST was also simulated using an analytical error of ± 0.01 ‰ for the $\delta^{18}O$ measurement and a SST calibration error of ± 2.5°C (Pagani et al., 1999). At each step of the pCO2 calculation, an additional 10,000 simulations were preformed for each sample to account for the following sources of uncertainty:

1) Analytical error of $\delta^{13}C$ of alkenone, randomly sampled with a Gaussian distribution with a standard deviation of ± 0.67 ‰
2) Analytical error of $\delta^{13}C$ of planktonic foraminifera, randomly sampled with a Gaussian distribution with a standard deviation of ± 0.05 ‰

3) Dissolved phosphate ($[PO_4^{3-}]$) (used to calculate b-factor), randomly sampled with a uniform distribution from 0.2 μM to 0.3 μMol

1 SD values for 1 and 2 were taken from Pagani et al. (1999). Propagating these sources of uncertainty, 68% and 95% confidence intervals for the pCO_2 estimate were then calculated using both the BAYSPAR and $\delta^{18}O$ SST proxies.

DATA REPOSITORY FIGURE CAPTIONS

(DR1) Data Repository Figure 1: Modern Atlantic SSTs in relation to location of drill sites discussed in this study. Modern mean annual sea surface temperatures from the World Ocean Atlas (2013) in the North Atlantic. The modern mean annual SST at Site 608 is ~16.7°C.

(DR2) Data Repository Figure 2: Age Model for Site 608. Datums include paleomagnetic reversals (Miller et al., 1991; Krijgsman et al., 2004), and datum levels from calcareous nannofossil biostratigraphy (Gartner, 1992; Olafson, 1991), and calcareous nannofossil and planktonic foraminiferal biostratigraphy (Di Stefano et al., 2011), using numerical ages from Gradstein et al. (2012).

(DR3) Data Repository Figure 3: Oxygen and carbon isotopes of foraminifera at Site 608 relative to the TEX_{86} record from this study. Planktonic and benthic foraminiferal oxygen and carbon isotopes from Site 608 relative to a global 'megasplice' (Miller et al., 1991; Pagani et al., 1999; Diester-Haass et al., 2009; De Vleeschouwer et al., 2017). Also plotted is the TEX_{86} index record from this study. The Miocene Climatic Optimum (brown) and Middle Miocene Climatic Transition (blue) are indicated.

(DR4) Data Repository Figure 4: Comparison of the BAYSPAR and TEX_{86}^{H} sea surface temperature calibrations. Average 'analog' BAYSPAR (blue line) and TEX_{86}^{H} (brown, dashed line) SST estimates plotted with 68% confidence intervals (Tierney and Tingley, 2015; Kim et al., 2010). BAYSPAR SST estimate are always cooler, with the difference ranging from ~2°C in the warmer part and ~4°C in the cooler part of the record.

(DR5) Data Repository Figure 5: Crossplots of TEX_{86}, $U^{k'}_{37}$ and GDGT source indices. BIT Index, Methane Index and Δ Ring Index are plotted relative to TEX_{86}, including data from stored (blue) and newly extracted samples (brown). The indices are not significantly correlated with TEX_{86} and, thus, sea surface temperature. Also shown is a cross plot of sea surface temperature estimates from BAYSPAR and $U^{k'}_{37}$, showing that BAYSPAR consistently estimates cooler SSTS (by up to 4°C) when $U^{k'}_{37}$ is below the calibration maximum.

(DR6) Data Repository Figure 6: Miocene record of TEX_{86}, BIT index, Methane Index and Δ Ring Index, alkenone $\delta^{13}C$ and εp change at Site 608. GDGT indices plotted on the depth scale, with numerical ages indicated. Raw 37:2 alkenone $\delta^{13}C$ values and εp calculated using SST estimates from 'analog' BAYSPAR calibration and $\delta^{18}O$ of surface dwelling planktonic foraminifera *(Globigerinoides spp*) are included in the bottom two panels. The interval from ~19.5 to ~17 Ma has variable 37:2 alkenone $\delta^{13}C$ values and is the interval of the highest and lowest pCO_2 estimates of the record. The Miocene Climatic Optimum (brown) and Middle Miocene Climatic Transition (blue) are indicated.

(DR7) Data Repository Figure 7: Miocene record of TEX_{86}, BIT Index and GDGT-2/GDGT-3 at Site 608. Higher values of GDGT-2/GDGT-3 suggest a greater contribution of GDGTs from deeper in the water column (Taylor et al., 2013); plotted on the depth scale, with numerical ages indicated. The Miocene Climatic Optimum (brown) and Middle Miocene Climatic Transition (blue) are indicated. Orange circles represent newly extracted samples while black circles are stored samples.

(DR8) Data Repository Figure 8: Glycerol dialkyl glycerol tetraether (GDGT) and alkenone abundances at Site 608, plotted on the depth scale, with numerical ages indicated. The top panel includes both branched (green line) and isoprenoidal (black line) GDGTs. Alkenone abundances (bottom panel) have the same general pattern as the GDGTs, although the absolute abundances are much lower (μg vs. ng). The Miocene Climatic Optimum (brown) and Middle Miocene Climatic Transition (blue) are indicated. Orange circles represent newly extracted samples while black circles are stored samples.

(DR9) Data Repository Figure 9: Temperature dependence of pCO_2 solubility. The temperature dependence of CO_2 solubility across a range atmospheric pCO_2 levels is plotted with the maximum and minimum dissolved CO_2(aq) estimates from Site 608. Sensitivity to SST variation is higher when dissolved or atmospheric CO_2 is elevated. Relationships calculated assuming constant salinity of 35 PSU from Weiss et al. (1974).

(DR10) Data Repository Figure 10: Analog BAYSPAR calibration grid cell map. The grid cells used to construct the linear BAYSPAR calibration are shown. Figure output from the MatLab BAYSPAR script (Tierney and Tingley, 2015).

TABLES DR1-DR3 CAPTIONS

(DR11) Table DR1: Fractional Glycerol Dialkyl Glycerol Tetraether (GDGT) abundances.

The fractional abundance of individual isoprenoidal GDGTs (GDGT-0, GDGT-1, GDGT-2,

GDGT-3, Crenarcheol (CREN) and the Crenarcheol regioisomer (CREN')) and branched

GDGTs (GDGT-1, GDGT-II, GDGT-III their respective isomer (a–c)). isoGDGT% represents

isoprenoidal GDGT abundance as a percentage of total isoprenoidal and branched GDGT abundance. Samples obtained in 2017 are indicated as 'new', those from Pagani et al. (1999) are designated 'stored.'

(DR12) Table DR2: Biomarker SST estimates from TEX_{86} and $U^{k'}_{37}$ and GDGT source indices. Some samples do not have measurements for both TEX_{86} and $U^{k'}_{37}$ due to low abundance of alkenones, and some missing samples of stored polar fractions. Calibrations used to calculate the $U^{k'}_{37}$ (Comte et al., 2006) and TEX_{86}^{H} (Kim et al., 2010) are shown, in addition to the 2.5th, 16th, 50th, 84th and 97.5th percentile predictions from the 'analog' BAYSPAR calibration used to calculate confidence intervals (Tierney and Tingley, 2015). GDGT source indices (BIT index (Weijers et al., 2007), Methane Index (Zhang et al., 2011), Δ Ring Index (Zhang et al., 2016) and GDGT-2/GDGT-3 (Taylor et al., 2013) are given, as well as the absolute concentration of a subset of samples measured by coinjection of the synthetic C46 standard (Huguet et al., 2006).

(DR13) Table DR3: Alkenone *p*CO2 calculation. Column titles described in DR. Calculations for the average sample *p*CO2 is shown, in addition to to 68% and 95% confidence interval calculated using a Monte Carolo approach to error propagation. Alkenone $\delta^{13}C$, foraminiferal $\delta^{13}C$ and foraminiferal $\delta^{18}O$ SST data from Pagani et al. (1999). *NOTE*: sea surface temperature estimates in **bold** use BAYSPAR SST values linearly interpolated from the next highest and next lowest sample as some samples with alkenone $\delta^{13}C$ lacked corresponding GDGT measurements. pCO_2 using TEX_{86}^{H} was not calculated for two samples (363.67 and 367.98 mbsf) with Methane Index values >0.5 (DR7).

DATA REPOSITORY REFERENCES

Bolton, C.T., Stoll, H.M. and Mendez-Vicente, A., 2012, Vital effects in coccolith calcite: Cenozoic climate-pCO2 drove the diversity of carbon acquisition strategies in coccolithophores?: Paleoceanography, v. 27, doi: 10.1029/2012PA002339.

Conte, M.H., Sicre, M.A., Rühlemann, C., Weber, J.C., Schulte, S., Schulz-Bull, D. and Blanz, T., 2006, Global temperature calibration of the alkenone unsaturation index ($U^{k'}_{37}$) in surface waters and comparison with surface sediments: Geochemistry, Geophysics, Geosystems, v. 7, p. 1-22, doi: 10.1029/2005GC001054.

De Jonge, C., Stadnitskaia, A. & Hopmans, E.C., 2014, In situ produced branched glycerol dialkyl glycerol tetraethers in suspended particulate matter from the Yenisei River, Eastern Siberia: Geochimica et Cosmochimica Acta, v. 125, p. 476-491, doi: 10.1016/j.gca.2013.10.031.

Fietz, S. et al., 2013, Eolian transport of glycerol dialkyl glycerol tetraethers (GDGTs) off northwest Africa: Organic Geochemistry, v. 64, p.112–118, doi: 10.1016/j.orggeochem.2013.09.009.

Henderiks, J. and Pagani, M., 2007, Refining ancient carbon dioxide estimates: Significance of coccolithophore cell size for alkenone-based pCO_2 records: Paleoceanography, v. 22, p. 1-12, doi: 10.1029/2006PA001399.

Huguet, C., Hopmans, E.C., Febo-Ayala, W., Thompson, D.H., Damsté, J.S.S. and Schouten, S., 2006, An improved method to determine the absolute abundance of glycerol dibiphytanyl glycerol tetraether lipids: Organic Geochemistry, v. 37, p.1036-1041, doi: 10.1021/ac062339v

Huguet, C., Kim, J.H., de Lange, G.J., Damsté, J.S.S. and Schouten, S., 2009, Effects of long term oxic degradation on the, TEX_{86} and BIT organic proxies: Organic Geochemistry, v. 40, p. 1188-1194, doi: 10.1016/j.orggeochem.2009.09.003.

Lengger, S.K., Hopmans, E.C., Damsté, J.S.S. and Schouten, S., 2012. Comparison of extraction and work up techniques for analysis of core and intact polar tetraether lipids from sedimentary environments. *Organic geochemistry*, *47*, pp.34-40.

Lengger, S.K., Hopmans, E.C., Damsté, J.S.S. and Schouten, S., 2014, Impact of sedimentary degradation and deep water column production on GDGT abundance and distribution in surface sediments in the Arabian Sea: Implications for the TEX_{86} paleothermometer: Geochimica et Cosmochimica Acta, v. 142, p. 386-399, doi: 10.1016/j.gca.2014.07.013.

Liu, Z., Pagani, M., Zinniker, D., DeConto, R., Huber, M., Brinkhuis, H., Shah, S.R., Leckie, R.M. and Pearson, A., 2009, Global cooling during the Eocene-Oligocene climate transition: Science, v. 323, p. 1187-1190, doi: 10.1126/science.1166368.

Liu, X.-L. et al., 2014, In situ production of branched glycerol dialkyl glycerol tetraethers in anoxic marine water columns: Marine Chemistry, v. 166, p.1–8, doi: 10.1016/j.marchem.2014.08.008.

Matthews, K.J., Maloney, K.T., Zahirovic, S., Williams, S.E., Seton, M. and Müller, R.D., 2016. Global plate boundary evolution and kinematics since the late Paleozoic: Global and Planetary Change, v. 146, p.226-250, doi.org/10.1016/j.gloplacha.2016.10.002

Pagani, M., Arthur, M.A. and Freeman, K.H., 1999, Miocene evolution of atmospheric carbon dioxide. Paleoceanography: v. 14, p. 273-292, doi: 10.1029/1999PA900006.

Pagani, M., Freeman, K.H. and Arthur, M.A., 2000, Isotope analyses of molecular and total organic carbon from Miocene sediments: Geochimica et Cosmochimica Acta, v. 64, p. 37-49, doi: 10.1016/S0016-7037(99)00151-9.

Pagani, M., 2014, 12.13 Biomarker-Based Inferences of Past Climate: The Alkenone pCO_2 Proxy: Treatise on Geochemistry. Elsevier, Oxford, p. 361-378.

Pagani, M., Zachos, J. C., Freeman, K. H., Tipple, B., Bohaty, S, 2005, Marked decline in atmospheric carbon dioxide concentrations during the Paleogene: Science, v. 309, p. 600-603, doi: 10.1126/science.1110063.

Rontani, J.F., Volkman, J.K., Prahl, F.G. and Wakeham, S.G., 2013, Biotic and abiotic degradation of alkenones and implications for paleoproxy applications: a review. Organic geochemistry, v. 59, p. 95-113, doi: 10.1016/j.orggeochem.2013.04.005.

Sales de Freitas, F., Pancost, R.D. and Arndt, S., The impact of alkenone degradation on $U^{k'}_{37}$ paleothermometry: a model-derived assessment: Paleoceanography, v. 32, p. 648-672 , doi: 10.1002/2016PA003043.

Schouten, S., Huguet, C., Hopmans, E.C., Kienhuis, M.V. and Sinninghe Damsté, J.S., 2007, Analytical methodology for TEX_{86} paleothermometry by high-performance liquid chromatography/atmospheric pressure chemical ionization-mass spectrometry: Analytical Chemistry, v. 79, p. 2940-2944, doi: 10.1021/ac062339v.

Smith, R.W., Bianchi, T.S. and Li, X., 2012, A re-evaluation of the use of branched GDGTs as terrestrial biomarkers: Implications for the BIT Index: Geochimica et Cosmochimica Acta, v. 80, p.14-29, doi: 10.1016/j.gca.2011.11.025.

Tierney, J.E. and Tingley, M.P., 2015, A TEX_{86} surface sediment database and extended Bayesian calibration: Scientific Data, v. 2, p. 150029, doi: 10.1038/sdata.2015.29.

Xiao, W., Wang, Y., Zhou, S., Hu, L., Yang, H. and Xu, Y., 2016, Ubiquitous production of branched glycerol dialkyl glycerol tetraethers (brGDGTs) in global marine environments: a new source indicator for brGDGTs: Biogeosciences, v. 13, p. 5883-5894, doi: 10.5194/bg-13-5883-2016.

Weijers, J.W., Schouten, S., van den Donker, J.C., Hopmans, E.C. and Damsté, J.S.S., 2007a, Environmental controls on bacterial tetraether membrane lipid distribution in soils: Geochimica et Cosmochimica Acta, v. 71, p. 703-713. , doi: 10.1016/j.gca.2006.10.003.

Weiss, R., 1974, Carbon dioxide in water and seawater: the solubility of a non-ideal gas, Marine chemistry: v. 2, p. 203-215, doi: 10.1016/0304-4203(74)90015-2.

Zell, C., Kim, J.H., Dorhout, D., Baas, M. and Damsté, J.S.S., 2015, Sources and distributions of branched tetraether lipids and crenarchaeol along the Portuguese continental margin:

Implications for the BIT index: Continental Shelf Research, v. 96, p. 34-44, doi: 10.1016/j.csr.2015.01.006.

Zhang, Y.G., Pagani, M. and Liu, Z., 2014, A 12-million-year temperature history of the tropical Pacific Ocean: Science, v. 344, p. 84-87, doi: 10.1126/science.1246172

Zhang, Y.G., Pagani, M., Liu, Z., Bohaty, S.M. and DeConto, R., 2013, A 40-million-year history of atmospheric CO_2: Phil. Trans. R. Soc. A, v. 371, p. 1-20, doi: 10.1098/rsta.2013.0096.

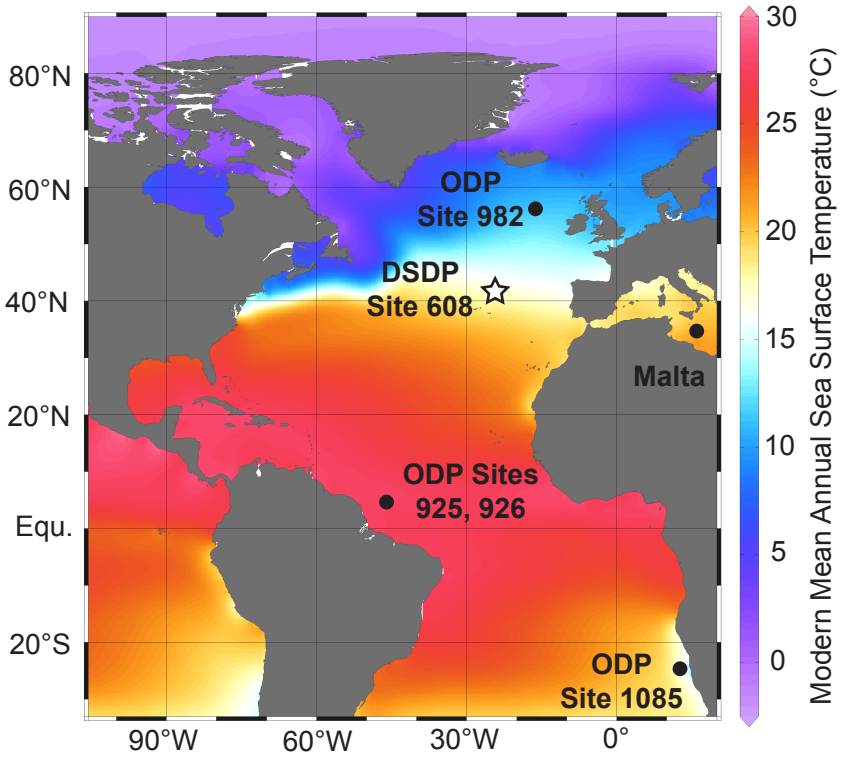

(DR1) Data Repository Figure 1: Modern Atlantic SSTs in relation to location of drill sites discussed in this study. Modern mean annual sea surface temperatures from the World Ocean Atlas (2013) in the North Atlantic. The modern mean annual SST at Site 608 is ~16.7°C.

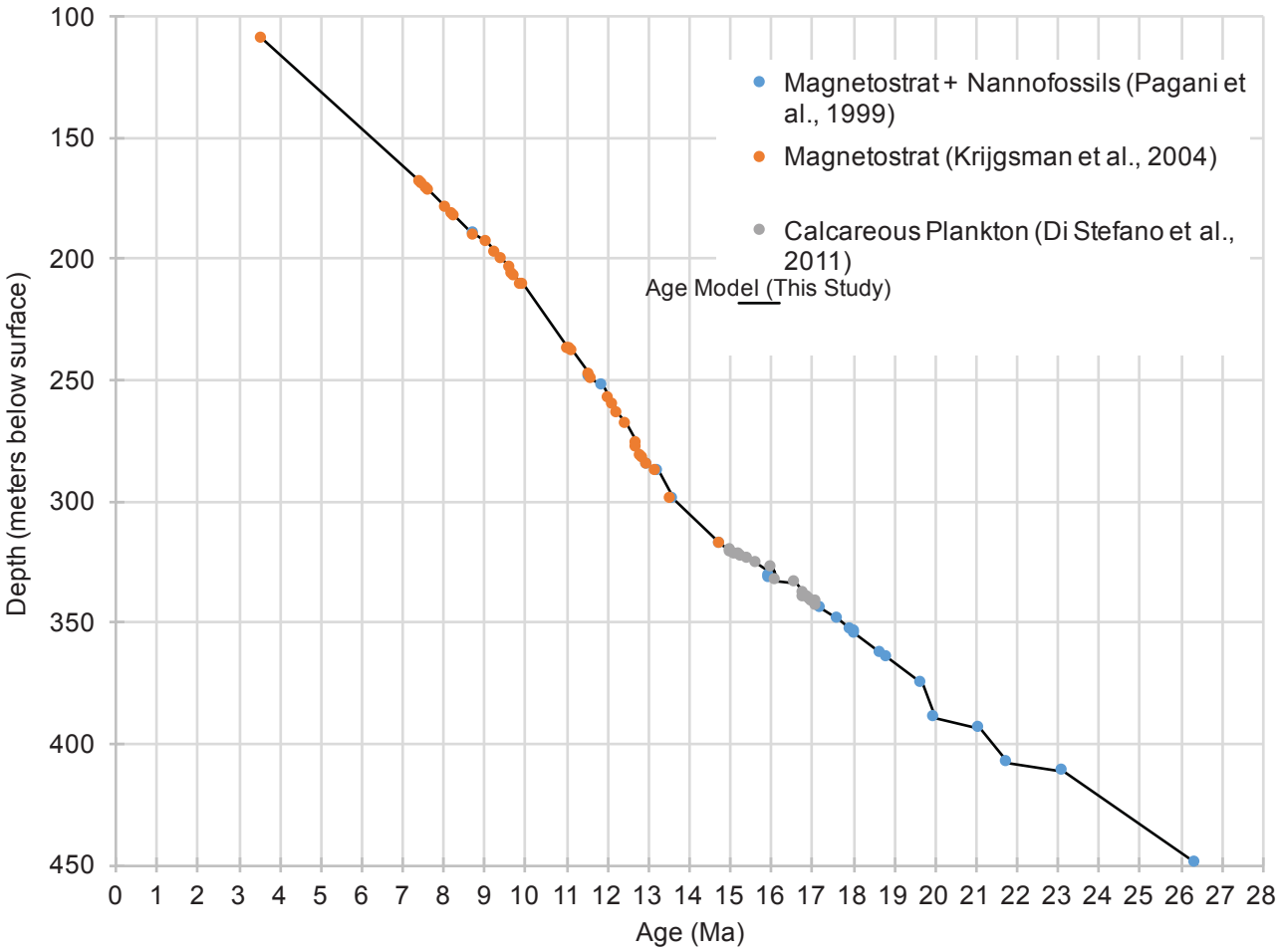

(DR2) Data Repository Figure 2: Age Model for Site 608. Datums include paleomagnetic reversals (Miller et al., 1991; Krijgsman et al., 2004), and datum levels from calcareous nannofossil biostratigraphy (Gartner, 1992; Olafson, 1991), and calcareous nannofossil and planktonic foraminiferal biostratigraphy (Di Stefano et al., 2011), using numerical ages from Gradstein et al. (2012).

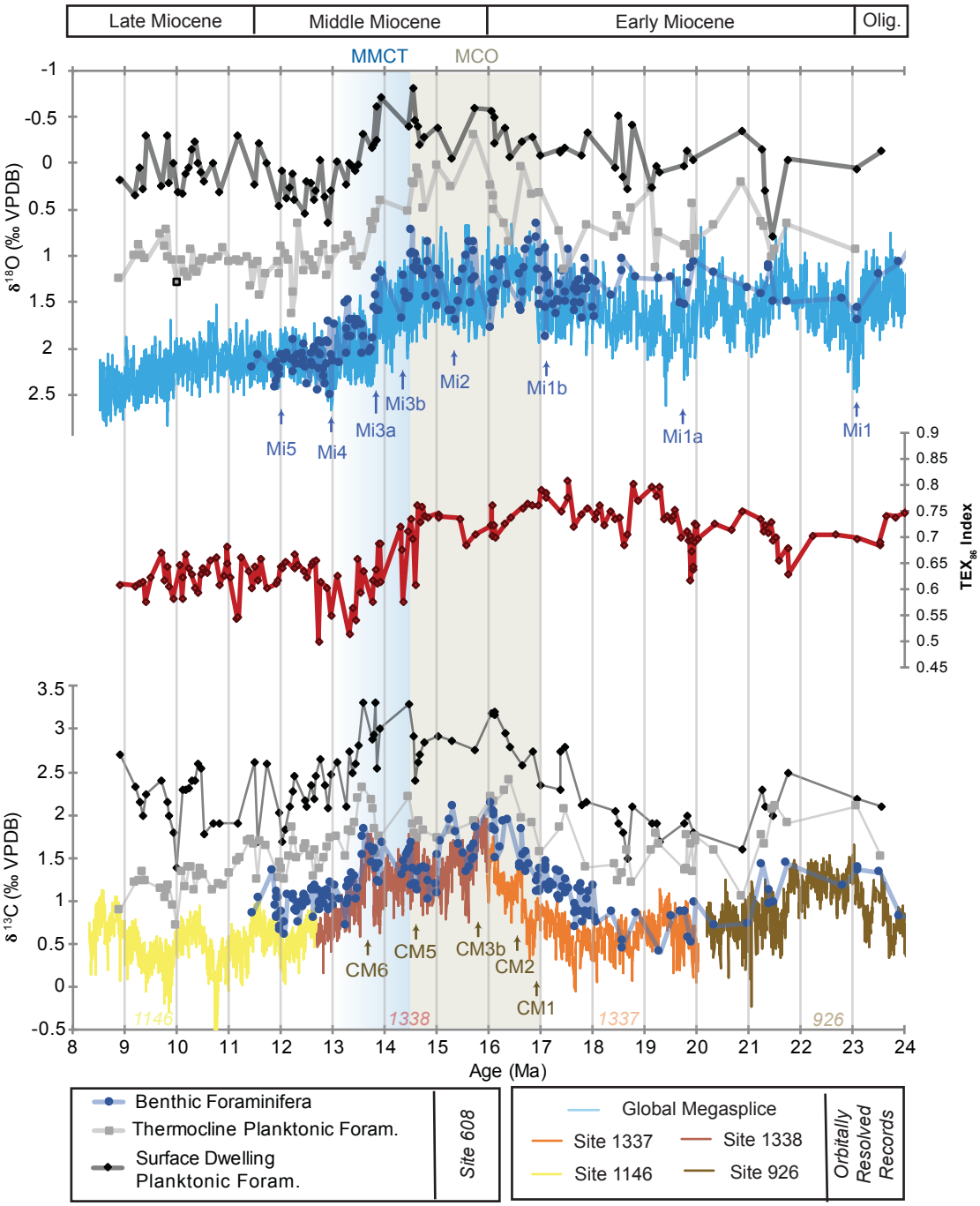

(DR3) Data Repository Figure 3: Oxygen and carbon isotopes of foraminifera at Site 608 relative to the TEX_{86} record from this study. Planktonic and benthic foraminiferal oxygen and carbon isotopes from Site 608 relative to a global 'megasplice' (Miller et al., 1991; Pagani et al., 1999; Diester-Haass et al., 2009; De Vleeschouwer et al., 2017). Also plotted is the TEX_{86} index record from this study. The Miocene Climatic Optimum (brown) and Middle Miocene Climatic Transition (blue) are indicated.

Data Repository
Figure 4 (DR4)

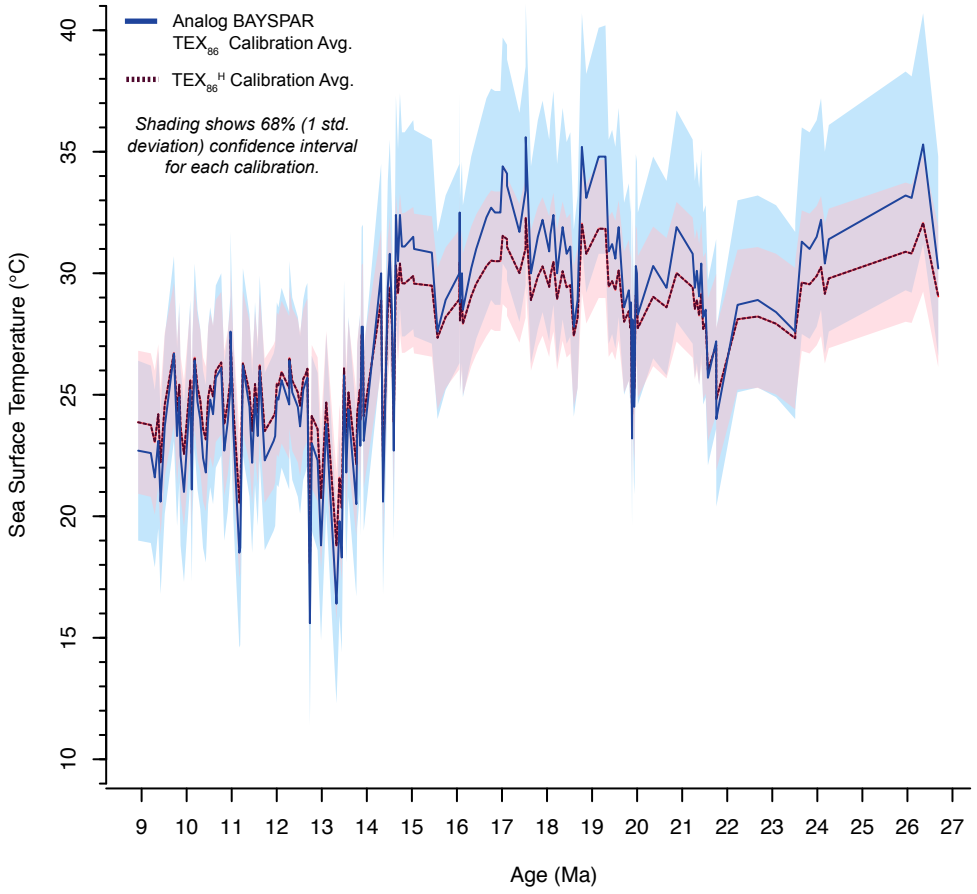

(DR4) Data Repository Figure 4: Comparison of the BAYSPAR and TEX_{86}^{H} sea surface temperature calibrations. Average 'analog' BAYSPAR (blue line) and TEX_{86}^{H} (brown, dashed line) SST estimates plotted with 68% confidence intervals (Tierney and Tingley, 2015; Kim et al., 2010). BAYSPAR SST estimate are always cooler, with the difference ranging from ~2°C in the warmer part and ~4°C in the cooler part of the record.

Miocene TEX_{86} and $U^{k'}_{37}$ sea surface temperature (SST) estimates at DSDP Site 608.

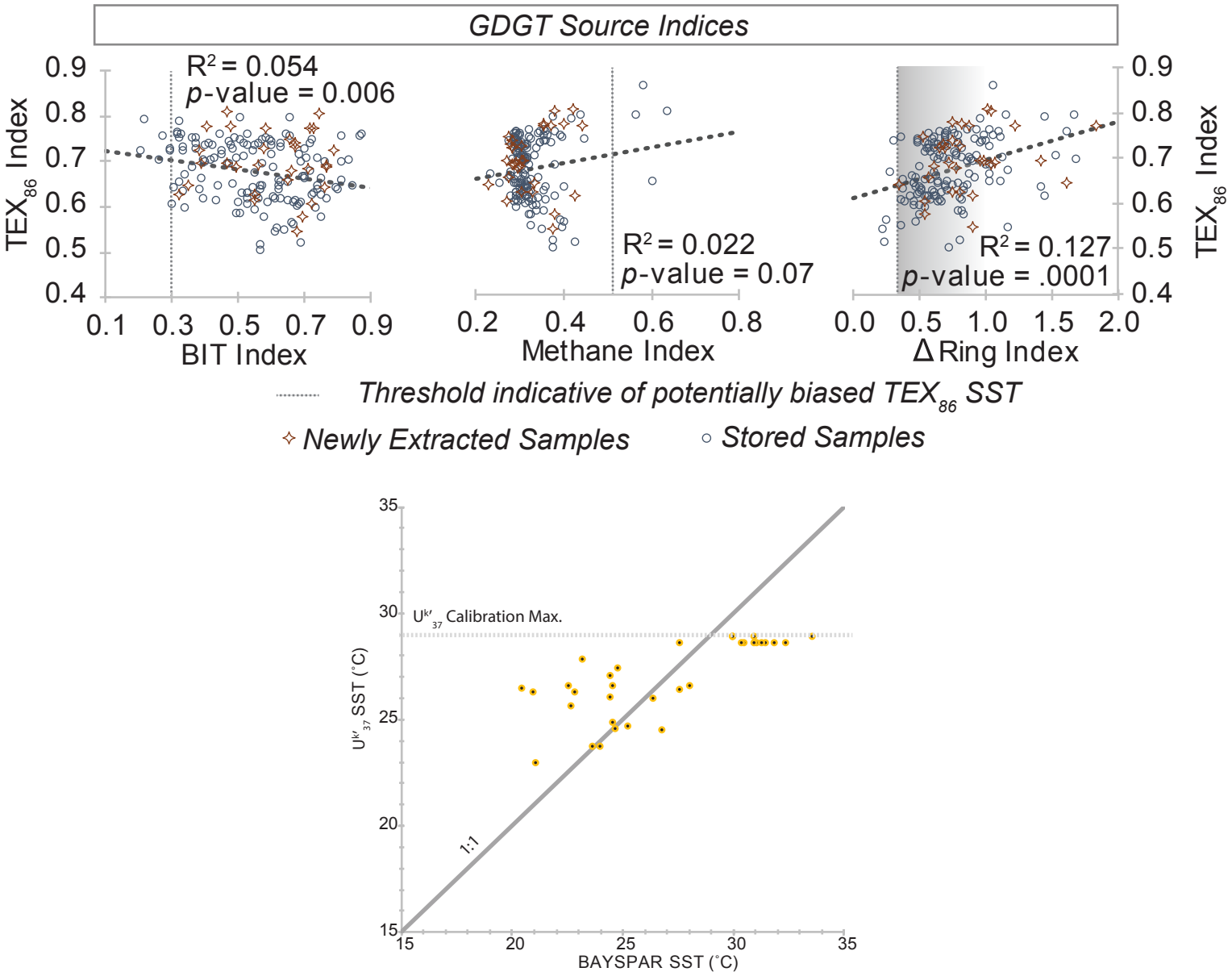

(DR5) Data Repository Figure 5: Crossplots of TEX_{86}, $U^{k'}_{37}$ and GDGT source indices. BIT Index, Methane Index and Δ Ring Index are plotted relative to TEX_{86}, including data from stored (blue) and newly extracted samples (brown). The indices are not significantly correlated with TEX_{86} and, thus, sea surface temperature. Also shown is a cross plot of sea surface temperature estimates from BAYSPAR and $U^{k'}_{37}$, showing that BAYSPAR consistently estimates cooler SSTS (by up to 4°C) when $U^{k'}_{37}$ is below the calibration maximum.

Data Repository
Figure 6 (DR6)

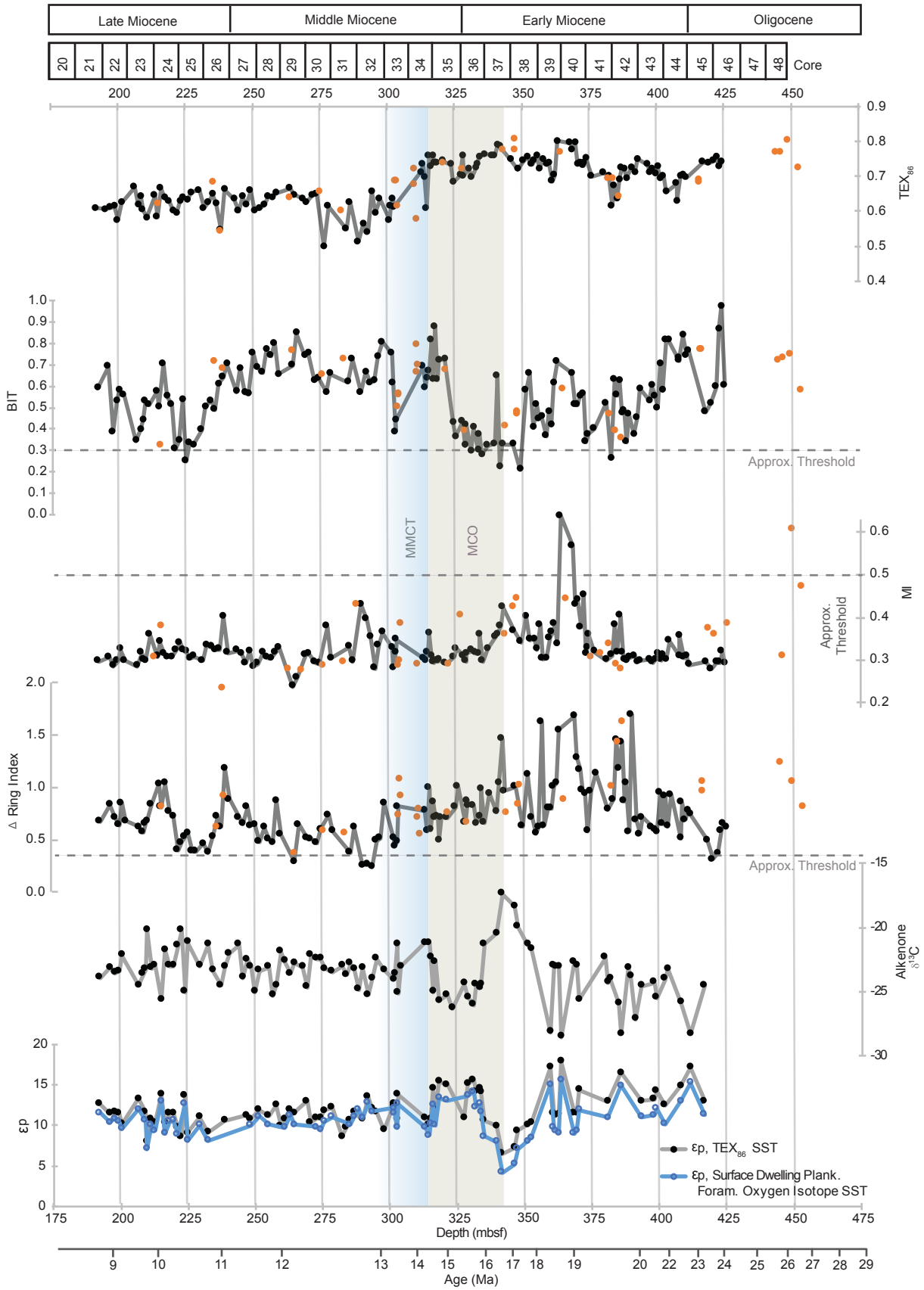

(DR6) Data Repository Figure 6: Miocene record of TEX_{86}, BIT index, Methane Index and Δ Ring Index, alkenone $\delta^{13}C$ and εp change at Site 608. GDGT indices plotted on the depth scale, with numerical ages indicated. Raw 37:2 alkenone $\delta^{13}C$ values and εp calculated using SST estimates from 'analog' BAYSPAR calibration and $\delta^{18}O$ of surface dwelling planktonic foraminifera *(Globigerinoides spp*) are included in the bottom two panels. The interval from ~19.5 to ~17 Ma has variable 37:2 alkenone $\delta^{13}C$ values and is the interval of the highest and lowest pCO_2 estimates of the record. The Miocene Climatic Optimum (brown) and Middle Miocene Climatic Transition (blue) are indicated.

Data Repository
Figure 7 (DR7)

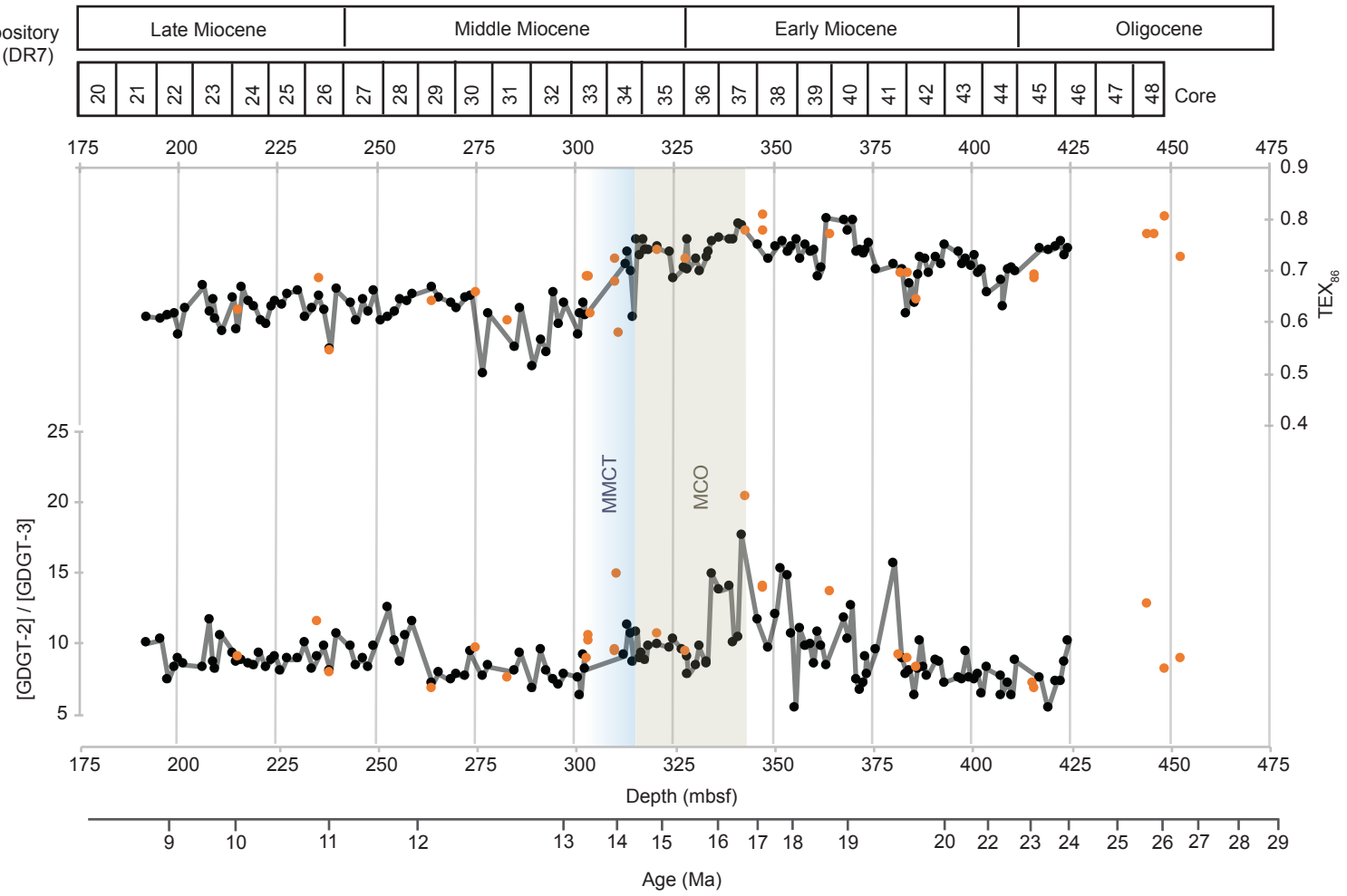

(DR7) Data Repository Figure 7: Miocene record of TEX_{86}, BIT Index and GDGT-2/GDGT-3 at Site 608. Higher values of GDGT-2/GDGT-3 suggest a greater contribution of GDGTs from deeper in the water column (Taylor et al., 2013); plotted on the depth scale, with numerical ages indicated. The Miocene Climatic Optimum (brown) and Middle Miocene Climatic Transition (blue) are indicated. Orange circles represent newly extracted samples while black circles are stored samples.

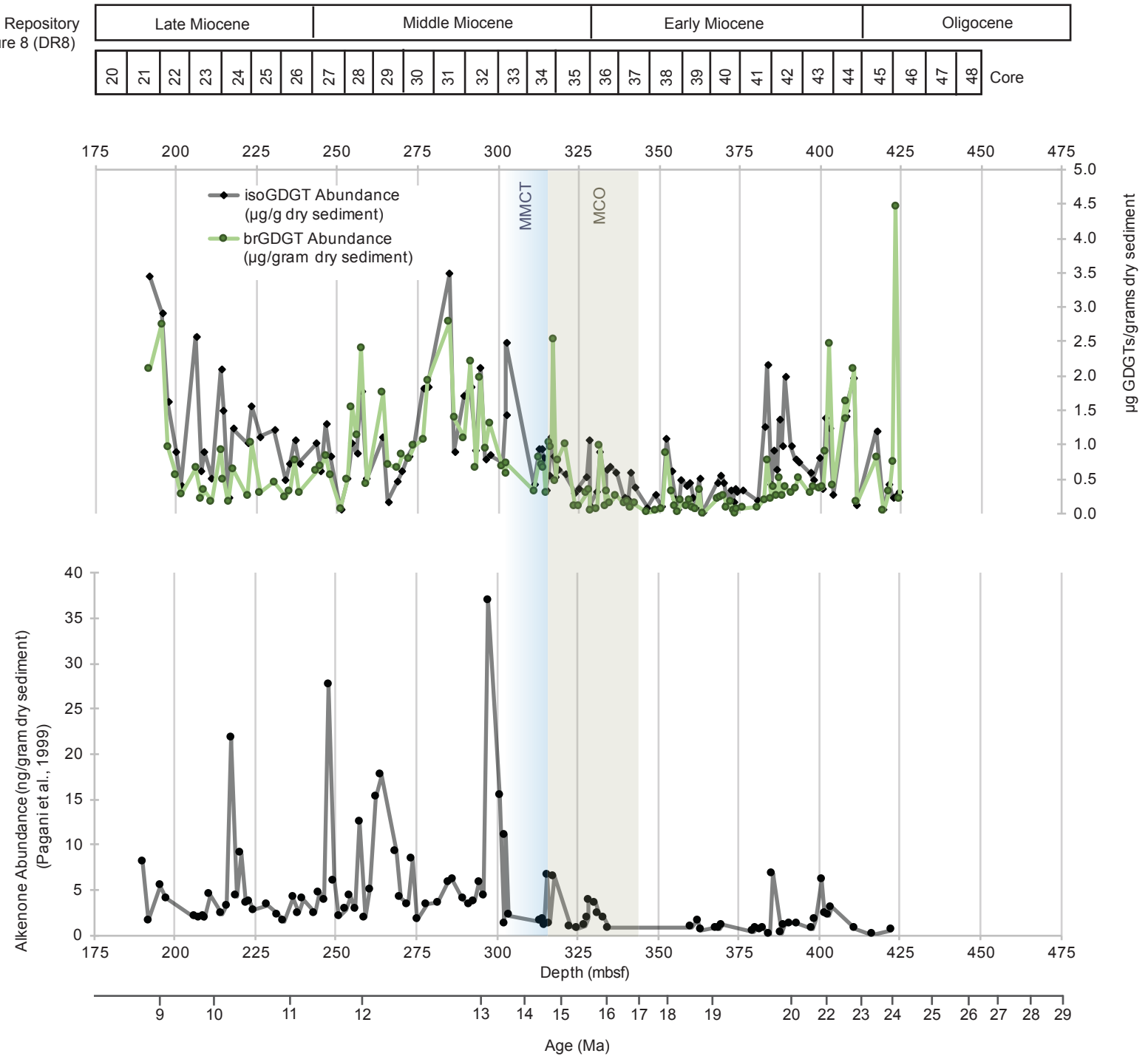

(DR8) Data Repository Figure 8: Glycerol dialkyl glycerol tetraether (GDGT) and alkenone abundances at Site 608, plotted on the depth scale, with numerical ages indicated. The top panel includes both branched (green line) and isoprenoidal (black line) GDGTs. Alkenone abundances (bottom panel) have the same general pattern as the GDGTs, although the absolute abundances are much lower (µg vs. ng). The Miocene Climatic Optimum (brown) and Middle Miocene Climatic Transition (blue) are indicated. Orange circles represent newly extracted samples while black circles are stored samples.

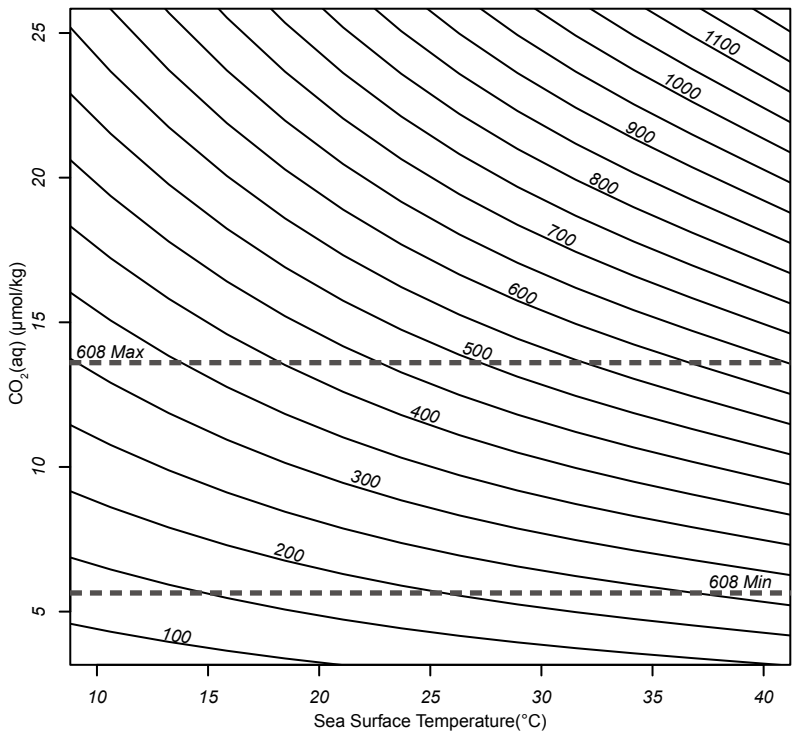

(DR9) Data Repository Figure 9: Temperature dependence of pCO_2 solubility. The temperature dependence of CO_2 solubility across a range atmospheric pCO_2 levels is plotted with the maximum and minimum dissolved CO_2(aq) estimates from Site 608. Sensitivity to SST variation is higher when dissolved or atmospheric CO_2 is elevated. Relationships calculated assuming constant salinity of 35 PSU from Weiss et al. (1974).

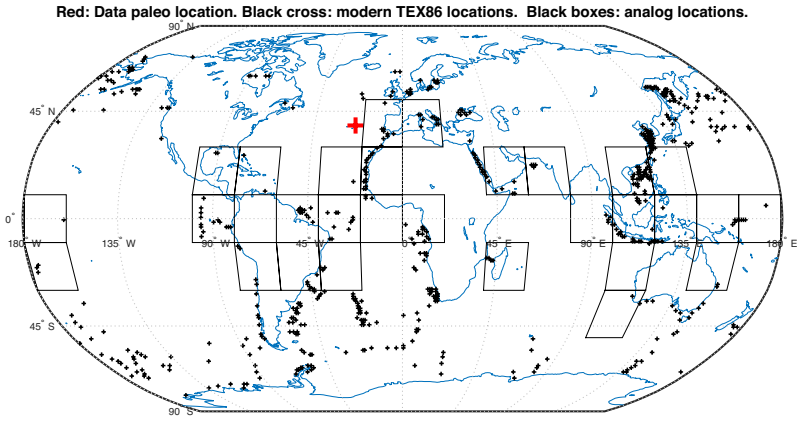

(DR10) Data Repository Figure 10: Analog BAYSPAR calibration grid cell map. The grid cells used to construct the linear BAYSPAR calibration are shown. Figure output from the MatLab BAYSPAR script (Tierney and Tingley, 2015).